nature communications

Article

https://doi.org/10.1038/s41467-025-59891-z

Mercapto-functionalized scaffold improves perovskite buried interfaces for tandem photovoltaics

Received: 25 November 2024

Accepted: 7 May 2025

Jianan Wang[1,2,12], Shuaifeng Hu[3,4,12], He Zhu[1,2,12], Sanwan Liu[1,12], Zhongyong Zhang[5,12], Rui Chen[1], Junke Wang[3], Chenyang Shi[1], Jiaqi Zhang[1], Wentao Liu[1], Xia Lei[6], Bin Liu[5], Yongyan Pan[1], Fumeng Ren[1], Hasan Raza[1], Qisen Zhou[1], Sibo Li[7], Longbin Qiu[7], Guanhaojie Zheng[8], Xiaojun Qin[9], Zhiguo Zhao[9], Shuang Yang[10], Neng Li[5], Jingbai Li[11], Atsushi Wakamiya[4], Zonghao Liu[1,2] ✉, Henry J. Snaith[3] ✉ & Wei Chen[1,2] ✉

Tandem photovoltaics hold great potential to surpass the efficiency limit of single-junction solar cells. Detrimental structural defects and chemical reactions at buried interfaces of subcells considerably impede the performance of integrated tandems. Here, we devise a mercapto-functionalized mesoporous silica layer as a superstructure at the buried interface to modulate the crystallisation, eliminate nanovoids, passivate defects, and suppress the oxidation of Sn(II) in the tin–lead perovskite films, contributing substantially to reduce charge carrier losses and improve stability in positive-intrinsic-negative structured devices. Consequently, the tin–lead perovskite single-junction cells show efficiency values of up to 23.7% with the best open-circuit voltage of 0.89 V. With the enhanced subcells, our double-junction tandems show efficiency values of 29.6% (certified 29.5% and steady-state 28.7%) and 24.7% on solar cells and 11.3 cm^2 mini-modules, respectively. Encapsulated tandems maintain 90% of initial efficiency after 445 h of maximum power point tracking under simulated 1-sun illumination.

All-perovskite tandems constructed with a wide-bandgap (WBG, ~1.80 eV), neat-lead perovskite, front subcell and a narrow-bandgap (NBG, ~1.25 eV), mixed tin–lead (Sn–Pb) perovskite, rear subcell offer superior strategy for new generation sustainable photovoltaics (PVs)[1–5]. The highest certified power conversion efficiency (PCE) of the all-perovskite tandem cells has just reached 30.1%[6], suggesting big room for improvement considering the theoretical maximum at ~45%[7]. To gain performance breakthroughs, fabricating high-quality WBG and NBG perovskite layers is critical. It was unveiled that the structural and electrical defects are primarily located at the top and buried (bottom)

---

[1]Wuhan National Laboratory for Optoelectronics, Huazhong University of Science and Technology, Wuhan, China. [2]Optics Valley Laboratory, Hubei, China. [3]Clarendon Laboratory, Department of Physics, University of Oxford, Oxford, UK. [4]Institute for Chemical Research, Kyoto University, Kyoto, Japan. [5]State Key Laboratory of Silicate Materials for Architectures, Wuhan University of Technology, Wuhan, China. [6]Department of Materials Science and Engineering, Southern University of Science and Technology, Shenzhen, China. [7]Shenzhen Key Laboratory of Intelligent Robotics and Flexible Manufacturing Systems, Department of Mechanical and Energy Engineering, SUSTech Energy Institute for Carbon Neutrality, Southern University of Science and Technology, Shenzhen, China. [8]Shanghai Synchrotron Radiation Facility (SSRF), Zhangjiang Lab, Shanghai Advanced Research Institute, Chinese Academy of Sciences, Shanghai, China. [9]Huaneng Clean Energy Research Institute, Beijing, China. [10]School of Materials Science and Engineering, East China University of Science and Technology, Shanghai, China. [11]Hoffmann Institute of Advanced Materials, Shenzhen Polytechnic University, Shenzhen, China. [12]These authors contributed equally: Jianan Wang, Shuaifeng Hu, He Zhu, Sanwan Liu, Zhongyong Zhang. ✉e-mail: liuzonghao@hust.edu.cn; henry.snaith@physics.ox.ac.uk; wnlochenwei@hust.edu.cn

surfaces of the perovskite layers in the device, leading to significant non-radiative charge carrier recombination and harmful chemical reactions[8–12]. It is therefore crucial to develop robust interface modification strategies, especially for Sn–Pb perovskites[13,14], considering its rapid crystallization and facile oxidation of Sn(II) to Sn(IV)[15–19]. On the other hand, in comparison to the readily post-treatable top interface, accessing the buried interface of the perovskite layer in devices is relatively challenging and less studied[9,14].

As for tin-containing perovskites, the current successful fabrication of efficient solar cells largely relies on the utilization of poly(3,4-ethylenedioxythiophene) polystyrene sulfonate (PEDOT:PSS) as the hole transport layer (HTL) and the substrate component for film deposition[10,12,20]. However, the acidity and hygroscopic nature of this material can induce undesirable oxidative reactions that drastically deteriorate the perovskite material and operational stability of its devices under elevated temperature and light illumination[21,22]. In addition, the possible spatial heterogeneity of PEDOT:PSS layer and the rapid growth of tin-based perovskites could lead to the generation of a high density of morphological nanovoids and crystallographic defects, unfavourable strain, and poor crystallinity at the buried interface[17,23,24]. In particular, eye-detectable white spots are found to be easy to form at the PEDOT:PSS/perovskite interface based on previous studies[17,23], and happened to be even more pronounced for films deposited on flat and smooth substrates, e.g., normally used indium tin oxide (ITO) glass. For single-junction cells, this issue could be mitigated by using a rough fluorine-doped tin oxide (FTO) glass substrate (~100 nm peak roughness)[17,23]. Unlike the perovskite-on-silicon tandem with pyramid architecture, the surface where the NBG Sn–Pb perovskite layer deposited, however, is—most of the time—very smooth WBG subcells in all-perovskite multijunction cells, posing additional challenges for mitigating the buried interface nanovoids and imperfections.

Bare this in mind, in this work, we devise a superstructure scaffold, composed of (3-mercaptopropyl)trimethoxysilane (MPTS) functionalized mesoporous silica nanoparticles (denoted as MSN-SH), to improve the buried interface of perovskite layers in tandem devices (Fig. 1a). Specifically, the silica nanoparticles primarily suppress the formation of nanovoids, release the residual strain, and improves the crystallinity of Sn–Pb perovskite films at the buried interface. The nucleophilic thiol end-groups at the scaffold surface of the substrate are designed to passivate the undercoordinated metal cations at the perovskite lattice and suppress the generation of iodide and oxidation of Sn(II). As a result, the NBG Sn–Pb perovskite solar cells (PSCs) show efficiency values of up to 23.7% and enhanced stability, especially under thermal conditions. In addition, this buried interface modification strategy also shows positive effects on neat lead perovskite materials under a series of bandgaps, i.e., 1.52, 1.68, and 1.77 eV. For instance, the resultant WBG, 1.77 eV, devices deliver efficiencies of up to 20.6%. With these improved subcells, the all-perovskite tandem devices show a certified PCE of 29.5% (certified steady-state PCE of 28.7%). Meanwhile, the modified tandems maintain 90% of their initial efficiency after 445 h of maximum power point tracking (MPPT) under simulated 1-sun illumination at room temperature and 82% of the initial efficiencies after 150 h of 85 °C thermal stressing.

Results and discussion

Improving substrate contact

We deposit the NBG mixed Sn–Pb perovskite films with a composition of $Cs_{0.1}FA_{0.6}MA_{0.3}Sn_{0.5}Pb_{0.5}I_3$ (FA: formamidinium, MA: methylammonium)[15]. Similar to previous reports[17], we observed distinct “white” spots viewed from the glass side of the perovskite films with ~900 nm in thickness on PEDOT:PSS-coated ITO substrate (Supplementary Fig. 1). This phenomenon was also observed for large-area Sn–Pb perovskite films processed via a vacuum-assisted crystallization procedure (Supplementary Fig. 2). We then prepare samples with the previously reported non-destructive peel-off method for scanning electron microscopy (SEM) characterizations to assess the morphology of buried interfaces[25] (Supplementary Fig. 3). Intriguingly, we detect dome-shaped nanovoids at the buried interface of Sn–Pb perovskite films which show “white” spots (Fig. 1b and Supplementary Figs. 4 and 5). A similar morphological characteristic is also observed for the Sn–Pb perovskite sub-absorber deposited on WBG subcell/PEDOT:PSS substrate during tandem cell fabrication (Supplementary Fig. 6). The appearance of such voids was previously reported for neat-Pb perovskites deposited from a dimethyl sulfoxide (DMSO)-containing solvent system and it appears to be more pronounced in thick and large-area perovskite films[26,27]. This phenomenon was attributed to the formation of an impermeable solid shell at the top of the “wet” films during a “top-down” crystallization of the films, leading to solvent-filled space at the buried interface and hence the formation of voids at the buried interface due to the film volume contraction after further solvent removal via annealing[28,29]. In our mixed Sn–Pb perovskite films, we find that only the specific combination of films with PEDOT:PSS substrate induced the formation of voids regardless of the thickness (Supplementary Fig. 1). We suppose that voids present at the buried interface might be associated with the spatial heterogeneity of PEDOT:PSS and/or unoptimized crystallization of perovskite films[17,23]. Furthermore, PEDOT:PSS is known to “swell” when coated in aprotic solvents such as *N*,*N*-dimethylformamide (DMF) and DMSO, which may also lead to additional solvent entrapping at this buried interface[30].

To address issues at this interface, we design a mesoporous silica nanoparticle (MSN)-constructed superstructure on PEDOT:PSS-based substrate before the deposition of perovskite films. The superstructure could serve as a nucleation seed of the perovskites deposited atop and hence contribute to the following crystallization process to improve buried interface[31–33]. We also find that further functionalization of MSN nanoparticles using MPTS, largely improves the dispersibility and stability of the MSN ink, which enables the deposition of a uniform superstructure with better reproducibility compared to Al_2O_3 and pristine MSN mesoporous scaffolds (Supplementary Note 1, Supplementary Figs. 7 and 8). Additionally, the essential characterization data of MSN nanoparticles before and after MPTS functionalization were summarized (Supplementary Note 2, Supplementary Figs. 9 and 10).

When integrated into the buried interface, the enhanced affinity and curvature of dispersed MSN-SH particles (~100 nm in size) lead to a decreased contact angle of the perovskite precursor solution with the substrate (Supplementary Fig. 11). This would affect the nucleation/growth of the perovskite films (Supplementary Note 3) and its quality. As shown in Fig. 1c and Supplementary Fig. 5f, the MSN-SH-based perovskite films show well-crystallized and dense domains without nanovoids. In addition, it is observed that the MSN-SH nanoparticles are nicely embedded into the perovskite bottom surface, and mainly located at the grain boundaries. These results suggest that the introduction of MSN-SH improves the quality of perovskite films, especially in the buried region, although there is no obvious change in the average grain size and surface roughness (Supplementary Figs. 12 and 13).

To further examine the effect of substrate on the crystallinity of perovskite films near the buried interface, we perform depth-resolved grazing incidence wide-angle X-ray scattering (GIWAXS) measurements at the exposed perovskite bottom surfaces, following film lift-off[34] (Fig. 1d, e). The MSN-SH-based Sn–Pb perovskite films show stronger diffraction intensity compared to the control under a series of tested incidence angles, suggesting a higher crystallinity and lower degree of amorphous phases (Supplementary Fig. 14). The reduced amorphous region could reflect the reduction in defect density at the bottom of the perovskite film[35]. We further evaluate the uniformity of the bottom interface using fluorescence lifetime imaging microscopy (FLIM) characterizations. The MSN-SH-based perovskite film exhibits a

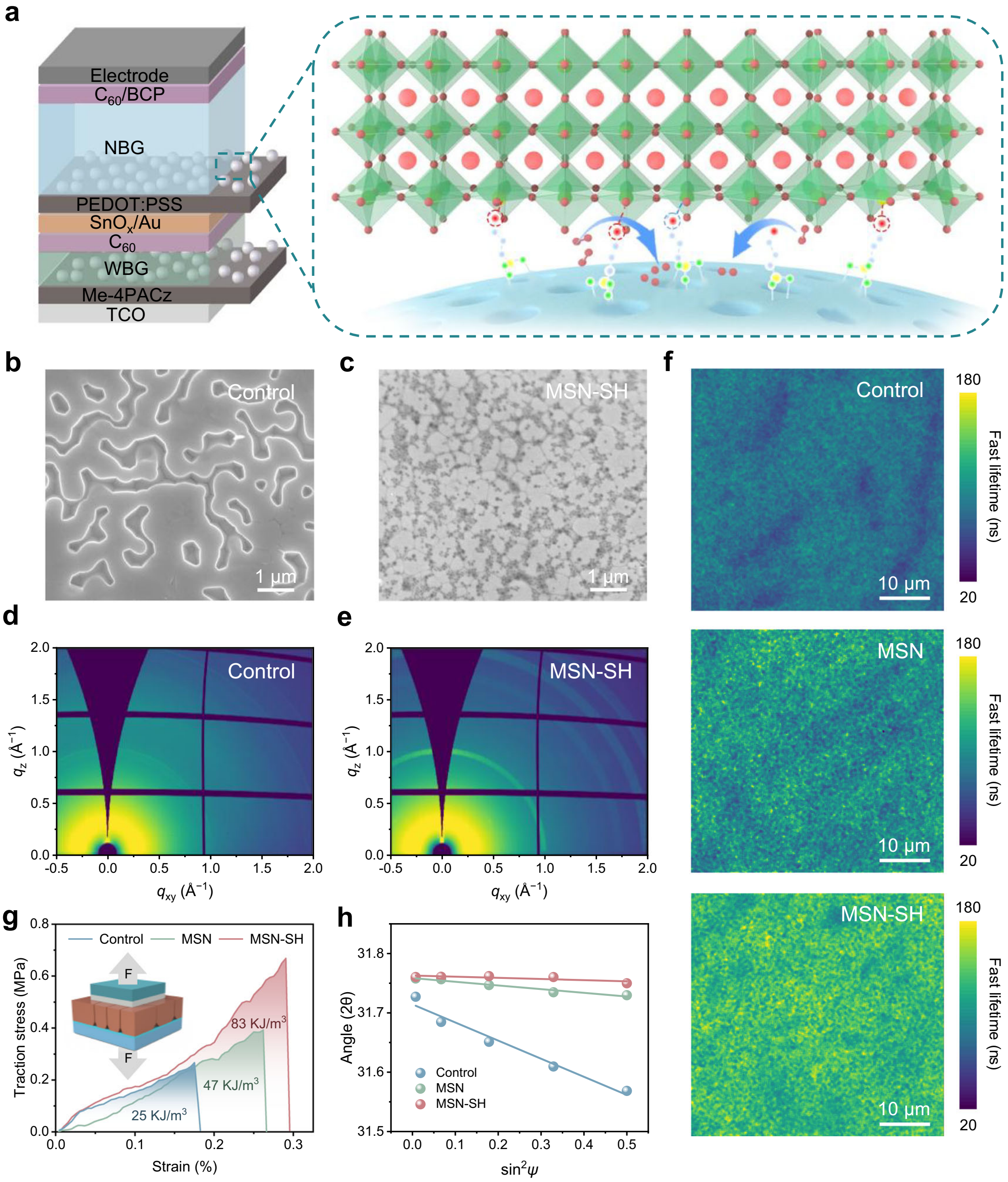

Fig. 1 | Characterizations of the buried interface. a Schematic diagram of the role of the MSN-SH layer in enhancing the stability of the buried interface. Top-view SEM images of the buried interface of perovskite films deposited on (**b**) ITO/PEDOT:PSS (control) and (**c**) ITO/PEDOT:PSS/MSN-SH (the MSN-SH sample) substrates. GIWAXS patterns collected on the exposed buried interface of (**d**) control and (**e**) MSN-SH perovskite films with an incidence angle of 0.1°. **f** FLIM measurements performed on the exposed buried interface of control, MSN, and MSN-SH perovskite films. **g** Stress-strain curve of the control, MSN, and MSN-SH perovskite device. (Inset) Experimental schematic for tensile stress measurement. **h** Residual strain analysis by linear fitting of 2θ-$\sin^2\psi$ for control, MSN, and MSN-SH perovskite films. Source data are provided as a Source Data file.

relatively uniform and enhanced photoluminescence (PL) lifetime over the probed region, 50 by 50 μm, indicating suppression of non-radiative recombination at the buried interface (Fig. 1f). Moreover, the presence of nanovoids and weaker crystalline amorphous phases at the buried interface often diminish the interfacial adhesion between the perovskite layer and the underlying substrate[25,36,37]. To validate the mechanical durability enhancement conferred by the MSN-SH superstructure at the buried interface, we conduct tensile strength measurements on the samples with a configuration of glass/ITO/PEDOT:PSS/perovskite/epoxy/glass. The stress-strain curves reveal the gradual evolution of the applied tensile stress versus strain until the occurrence of delamination (Fig. 1g)[37]. The critical tensile strength of the perovskite/PEDOT:PSS interface is determined to be 0.26 MPa at 0.17% strain for the control sample and 0.67 MPa at 0.29% strain for the MSN-SH sample. The determined specific fracture energy increases from 25 to 83 kJ m^{-3}, thanks to the elimination of nanovoids and the promotion of cohesive adhesion by the MSN-SH superstructure. As previously reported, the improvement of the buried interface contact could assist in the release of residual stress for perovskite films[25]. We thus conduct grazing-incidence X-ray diffraction (GIXRD) measurements at an incidence angle of 0.3° to examine the residual stress state of the exfoliated samples at the macroscopic level (Supplementary Fig. 15). The results show that the control film presents tensile stress at the region near PEDOT:PSS layer, while the insertion of MSN-SH

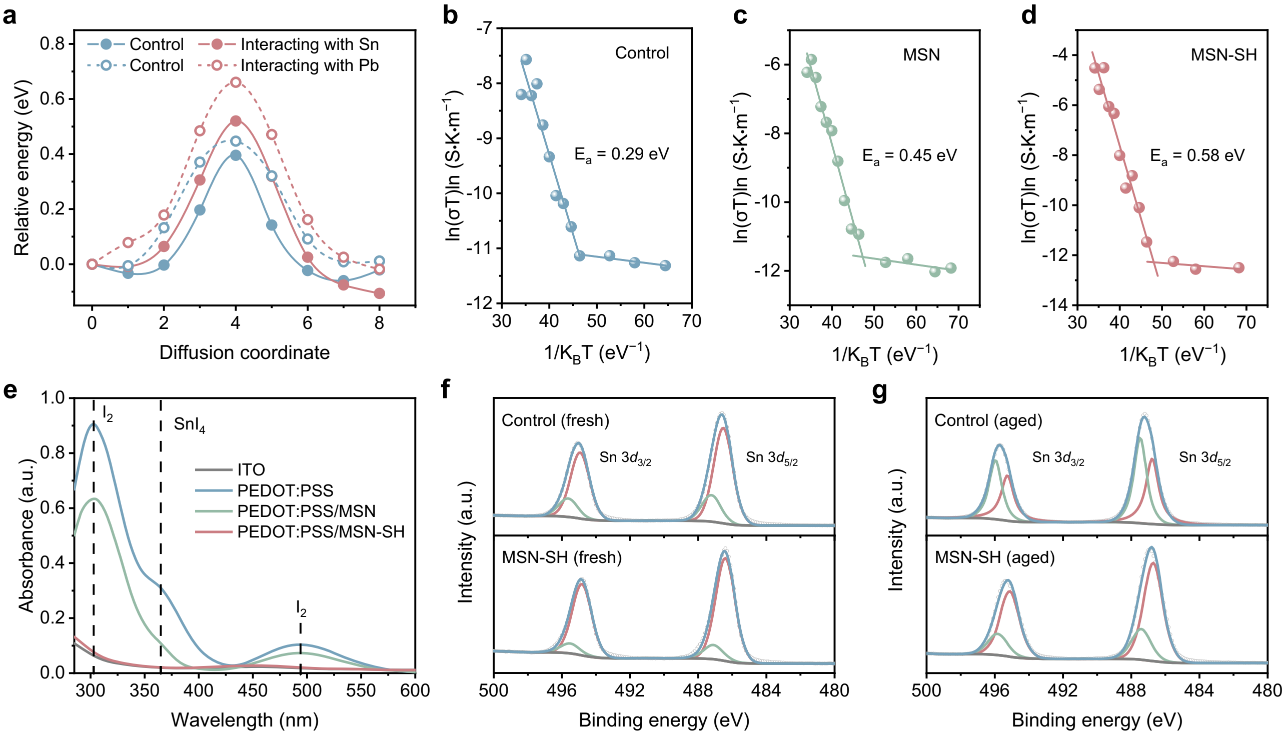

Fig. 2 | Stability of the buried interface. a V_I migration energy barriers in the control and butanethiol systems interacting with Pb(II) and Sn(II) in the perovskite lattice. Temperature-dependent dark conductivity results of (**b**) control, (**c**) MSN, and (**d**) MSN-SH perovskite films. **e** Absorbance spectra of toluene solutions in which the perovskite films deposited on ITO, PEDOT:PSS, PEDOT:PSS/MSN or PEDOT:PSS/MSN-SH substrates aged at 85 °C for 48 h. XPS spectra of Sn 3*d* core levels performed on the peeled surface of the control and MSN-SH films (**f**) before and (**g**) after simulated AM1.5G illumination for 240 h under N_2. Source data are provided as a Source Data file.

material effectively releases the stress from 72.2 down to 4.6 MPa (Fig. 1h and Supplementary Note 4). We speculate that this released residual stress is mainly associated with the elimination of nanovoids and enhanced interaction at the buried interface[36,38].

It was reported that the widely used [4-(3,6-dime-thyl-9H-carbazol-9-yl)butyl]phosphonic acid (Me-4PACz) material bearing nonpolar methyl terminal groups leads to a surface with insufficient wettability for solution processing, resulting in poor coverage of perovskite films (Supplementary Fig. 16)[39,40]. Interestingly, the Me-4PACz/MSN-SH bilayer substantially alleviated this wetting issue, yielding well-covered perovskite films. We also find that the introduction of MSN-SH as a meso-superstructure ensures homogeneous and compact films with no detectable nanovoids at the bottom interface of the neat lead films (Supplementary Fig. 17). This result suggests good compatibility of MSN-SH superstructure in both Sn–Pb and Pb perovskites for improved buried interface contact and film quality.

Enhancing interface stability

Based on the understanding of the buried interface degradation mechanisms, we expect the potential capability of our MSN-SH approach to enhance the stability of the buried interface by reducing the concentration of Sn (V_{Sn}) and iodide (V_I) vacancies. We propose that the potential chelating between the sulfhydryl group and metal cations, i.e., Sn(II) and Pb(II), from the perovskites, and the reducibility of the sulfhydryl group[41] at the surface of the MSN-SH superstructure, will increase the iodide migration energy and impede the generation of oxidative I_2.

To verify this, we first perform the density functional theory (DFT) calculations to evaluate the V_I formation energy and the iodide migration barrier when the sulfhydryl group binds to the perovskite framework. To simplify the model, we refer to the previous report using butanethiol[42] to represent MSN-SH. From the calculation results, we find that the V_I formation energy increases from about 1.70 to about 2.15 eV when the sulfhydryl group binds to Pb-I or Sn-I terminals (Supplementary Fig. 18). The I^- migration barrier also increases from 0.45 to 0.66 eV and 0.40 to 0.45 eV in the case of Pb-I and Sn-I terminals, respectively (Fig. 2a and Supplementary Fig. 19). To experimentally verify the increase of ion migration active energy, we further measure the temperature-dependent conductivity of the films (Fig. 2b–d). The activation energy for MSN-SH films is calculated to be 0.58 eV, twice that of the control, 0.29 eV. We in addition verify that MSN-SH should be capable of reducing and suppressing the formation of I_2 and Sn(IV) in Sn–Pb perovskites (Supplementary Note 5, Supplementary Figs. 20 and 21).

To investigate further with a practical scenario, we immerse Sn–Pb perovskite films deposited on different substrates into toluene and measure the ultraviolet-visible (UV–Vis) absorption of the solution. This method enables the “collection” of toluene dissolvable degradation products, i.e., I_2 and SnI_4. After 48 h of 85 °C heating, the toluene solutions are then subjected to absorption measurement to trace the generation of possible decomposition products giving characteristic peaks. As indicated by the absorbance, we observe a significant amount of I_2 and SnI_4 species released from the perovskite films deposited on PEDOT:PSS substrates. In contrast, no notable I_2 and SnI_4 absorption sources from the solutions containing PEDOT:PSS/MSN-SH-based films (Fig. 2e and Supplementary Fig. 22). The results suggest that Sn–Pb perovskite films deposited on untreated PEDOT:PSS deteriorate at an elevated temperature, whereas this degradation appears to be greatly suppressed in MSN-SH case. We further conduct X-ray photoelectron spectroscopy (XPS) measurements to analyse the chemical valence state of Sn at the peeled surface of films before and after 240 h of illumination. The results show that the Sn(IV) content decreased from 21.8 to 12.6% and 55.6 to 23.8% for the fresh and aged samples, respectively, upon MSN-SH treatment,

https://doi.org/10.1038/s41467-025-59891-z

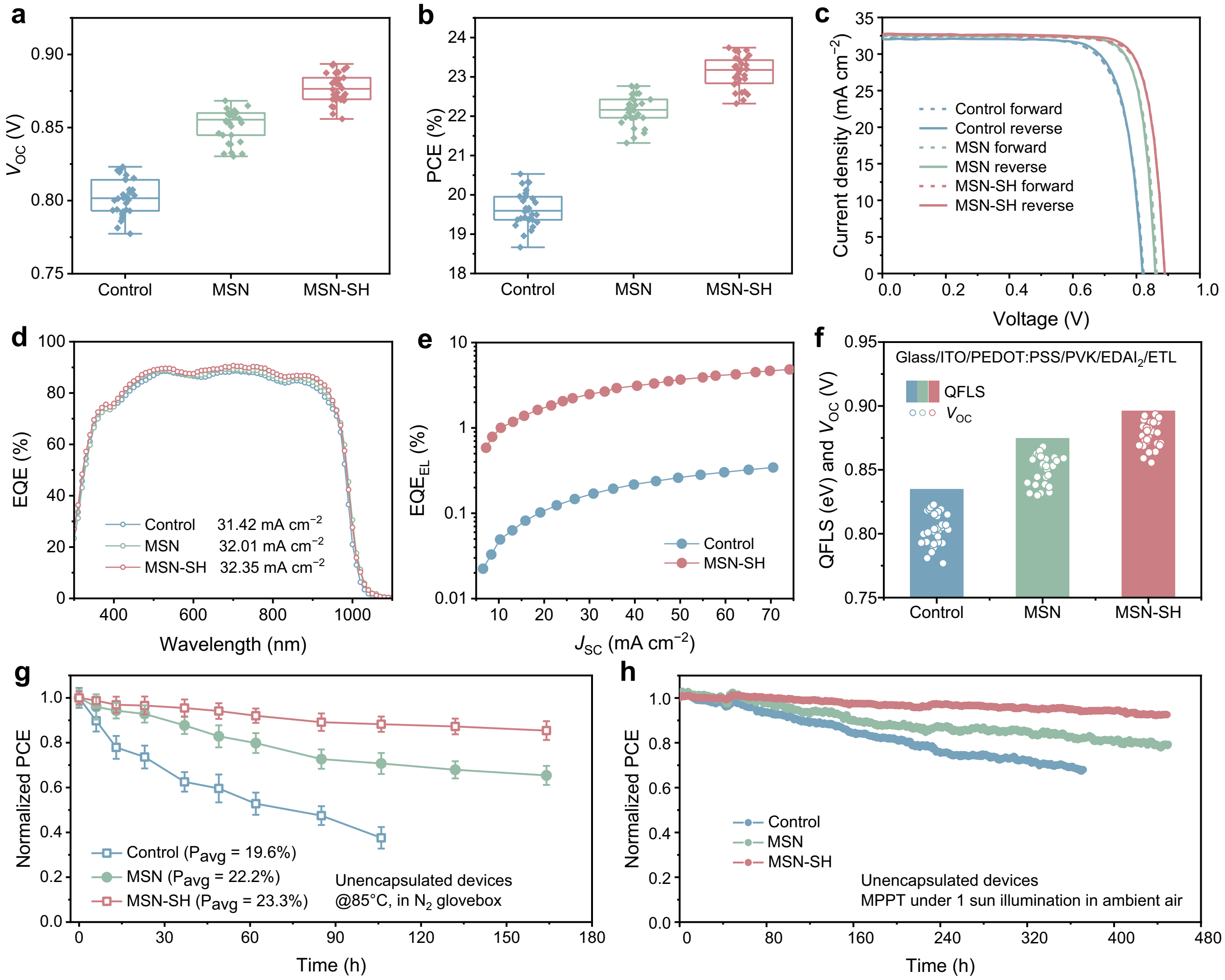

Fig. 3 | Performance and characterization of Sn–Pb PSCs. Statistical distribution of (**a**) V_{OC} and (**b**) PCE for control, MSN, and MSN-SH Sn–Pb PSCs based on 30 devices. **c** J–V curves of champion control, MSN, and MSN-SH device under reverse and forward scans. **d** The EQE spectra of control, MSN and MSN-SH devices. **e** Electroluminescence quantum efficiency versus current density for control and MSN-SH devices. **f** Comparison of V_{OC} extracted from the J–V curves of the device with the corresponding QFLS of representative layer stacks. **g** Performance evolution of unencapsulated control, MSN, and MSN-SH Sn–Pb PSCs aged at 85 °C under dark in the N_2 glovebox. **h**, Continuous MPPT for the encapsulated control, MSN, and MSN-SH Sn–Pb PSCs under simulated AM1.5G illumination in ambient air. Source data are provided as a Source Data file.

suggesting the greatly suppressed oxidation of Sn(II) in the buried region of perovskite films even under elevated temperature (Fig. 2f, g, and Supplementary Table 1).

Single-junction devices

Encouraged by the enhanced buried interface with the MSN-SH modification, we fabricate single-junction Sn-Pb cells with an architecture of ITO/PEDOT:PSS/perovskite/ethylenediammonium diiodide ($EDAI_2$)[17]/C_{60}/bathocuproine (BCP)/Ag. Based on the device results, the application of MSN-SH improves the V_{OC} and fill factor (FF), where the average V_{OC} is boosted from 0.802 V to 0.877 V. The MSN-SH devices thus show a considerably enhanced average PCE of 23.1% compared to that of the control, 19.6% (Fig. 3a, b, Supplementary Fig. 23 and Supplementary Table 2). The MSN-SH devices also show negligible hysteresis, with the best PCE values of 23.7% (steady-state PCE of 23.3%, V_{OC} of 0.887 V, J_{SC} of 32.8 mA cm^{-2}, and FF of 81.7% under reverse scan, Fig. 3c and Supplementary Fig. 24), representing one of the best results reported in the field[10,17,43]. Integrating the external quantum efficiency (EQE) spectra with AM1.5G spectrum gives J_{SC} values of 31.4 and 32.4 mA cm^{-2} for the control and MSN-SH cells, respectively (Fig. 3d).

With solar cells, we further conduct transient photocurrent decay (TPC), transient photovoltage decay (TPV), and external quantum efficiency of electroluminescence (EQE$_{EL}$) measurements. The current decay lifetime decreases from 3.86 to 2.37 μs, while the voltage decay lifetime increases from 149 to 626 μs, for the control and MSN-SH devices, respectively. These results suggest that the MSN-SH buried interface modification facilitates charge carrier extraction while suppressing interface recombination (Supplementary Figs. 25 and 26), which is further rationalised by the decreased dark saturation-current density and device ideality factor along with the enhanced built-in potential (V_{bi}) (Supplementary Figs. 27 and 28). On the other hand, the EQE$_{EL}$ results suggest an increase by a factor of ~13 at the current injection level close to the device J_{SC}, upon MSN-SH modification (0.20% vs 2.61%, Fig. 3e). The calculated non-radiative recombination loss is reduced by ~70 mV, in close agreement with the improved device V_{OC}[44,45] (Supplementary Note 6, Supplementary Fig. 29a and Supplementary Table 3). We also observe that the improved FF considerably originates from minimized non-radiative recombination loss, attributing likely to the reduced interface defects[32,46] (Supplementary Fig. 29b).

We further measure the photoluminescence quantum yield (PLQY) for neat perovskite, HTL/perovskite, and HTL/perovskite/$EDAI_2$/ETL samples to estimate the quasi-Fermi level splitting (QFLS) and voltage losses. We find that MSN-SH significantly reduces the contact loss caused by PEDOT:PSS layer while enhancing the PLQY value of neat perovskite films (Supplementary Figs. 30, 31 and Supplementary Table 4). Comparing the differences between the calculated QFLS values for the PEDOT:PSS/perovskite/$EDAI_2$/C_{60} stacks and the V_{OC} extracted from the J–V measurements suggests the critical role of MSN-SH layer in reducing the QFLS-V_{OC} mismatch (Supplementary Note 7, Fig. 3f and Supplementary Fig. 32).

Ageing the devices under 85 °C, the MSN-SH-based samples retain 85% of the initial efficiency after 164 h (Fig. 3g), however, the control devices show rapid loss, 38% retained in 106 h. Additionally, the MSN-SH-based device also exhibits promising operational stability under MPPT conditions (Fig. 3h) with 93% of its initial efficiency retained after over 450 h, considerably better than 68% after 370 h for the control device. These results suggest that our MSN-SH buried interface modification is a robust strategy for improving the thermal or operational stability of devices (Supplementary Note 8, Supplementary Fig. 33).

To further test the universality of the MSN-SH treatment, we select the neat lead PSCs with bandgaps of 1.52, 1.68, and 1.77 eV to study. Compared to control devices, MSN-SH devices exhibit considerably higher PCE and V_{OC} values along with better reproducibility, suggesting the compatibility of MSN-SH in improving p-i-n perovskite devices (Supplementary Fig. 34-36). In particular, the 1.77 eV WBG PSCs achieve a PCE of up to 20.6% with V_{OC} of 1.33 V, J_{SC} of 18.3 mA cm^{-2}, and FF of 84.7%, in line with the certified results (Supplementary Fig. 37 and Supplementary Table 5).

To evaluate the photoinduced phase segregation of mixed halide perovskite (1.77 eV, $FA_{0.8}Cs_{0.2}Pb(I_{0.6}Br_{0.4})_3$), we perform the time-dependent PL measurements (Supplementary Fig. 38). We observe severe halide segregation for the control film, suggested by the multiple emission peaks deconvoluted from the PL under an elongated illumination. On the contrary, the MSN-SH-modified film maintains the PL shapes relatively well, with only a slight peak shift present during the period of exposure. This suppressed halide segregation might benefit from the improved interface quality and the release of lattice strain via the MSN-SH modification (Supplementary Fig. 39).

Tandem devices

With the improved NBG and WBG perovskite subcells, we further fabricate monolithic two-terminal tandems with a device configuration of ITO/Me-4PACz/MSN-SH/WBG perovskite (~350 nm)/1,3-propanediamine dihydriodide ($PDAI_2$)[11]/C_{60}/SnO_x/Au (1 nm)/PEDOT:PSS/MSN-SH/NBG perovskite (~900 nm)/$EDAI_2$/C_{60}/BCP/Ag. The cross-section SEM image of the device is shown in Fig. 4a. Benefiting from the concurrent reduction of non-radiative recombination loss in both WBG and NBG subcells, the MSN-SH tandem devices exhibit significant improvement in FF and V_{OC} compared to the control (Fig. 4b, Supplementary Table 6). As shown in Fig. 4c, the champion MSN-SH cell exhibits negligible hysteresis under forward and reverse scans. The device PCE reaches 29.6% from the reverse scan, with a V_{OC} of 2.18 V, a J_{SC} of 16.3 mA cm^{-2}, an FF of 83.4%, and a steady-state PCE of 29.1% after a 300 s operation (Supplementary Fig. 40). The J_{SC} values obtained by integrating the EQE spectra of WBG and NBG subcells are 16.3 and 16.0 mA cm^{-2}, respectively (Fig. 4d). We then send our tandems to an accredited independent laboratory (Shanghai Institute of Microsystem and Information Technology, SIMIT, Shanghai, China) for certification, providing PCE of 29.50% (V_{OC} of 2.179 V, J_{SC} of 16.25 mA cm^{-2} and FF of 83.29%), and maximum power point efficiency of 28.7% (Supplementary Fig. 41). Encouragingly, this is one of the highest performance values reported for the monolithic two-terminal all-perovskite tandems, to the best of our knowledge[6]. We further fabricate 34 MSN-SH-based tandem mini-modules on 5 × 5 cm^2 substrates with a subcell width of 6.8 mm and a dead-area width of 300 μm, resulting in a geometry FF of 96.4% (Supplementary Fig. 42). The tandem mini-modules show an average PCE of 24.2% and a best value of 24.7% (Fig. 4e and Supplementary Table 7), suggesting a superior upscaling potential of our MSN-SH buried interface modification for multi-junction devices.

We then examine the thermal stability of tandem cells and find that the MSN-SH-based devices maintain 82% of their initial PCEs over 150 h under 85 °C ageing, whereas the control devices retain only 43% of their initial PCEs after 100 h (Supplementary Fig. 43). We also perform MPPT tests for encapsulated tandems under continuous simulated AM1.5 G illumination in ambient conditions (Fig. 4f and Supplementary Fig. 44). The MSN-SH-based tandem cell maintains over 90% of the initial efficiency after over 430 h of operation, largely surpassing control cell at 75% in 325 h. The encapsulated MSN-SH mini-module could also maintain over 80% of the initial efficiency after over 290 h of continuous operation.

In summary, we have shown a designed (3-mercaptopropyl)trimethoxysilane-functionalized scaffold to allow the deposition of high-quality NBG Sn–Pb perovskite films with a nanovoid-free buried interface. The resulting films exhibit reduced structural defects, suppressed ion migration, released lattice strain, and minimized interface recombination. With the optimized buried interface, a PCE of 23.7% is obtained for the NBG PSCs with a V_{OC} of up to 0.89 V. We also demonstrate that this buried interface modification method is effective for the fabrication of 1.77 eV WBG PSCs, achieving a PCE of up to 20.6% with a V_{OC} of 1.33 V. With the improved subcells, the integrated all-perovskite tandem cells have demonstrated a certified PCE of 29.5% (certified steady-state PCE of 28.7%), along with enhanced stability. We believe that the design strategy provides valuable insights for the community in developing functional superstructures that can precisely modulate the buried interface for solar cells and other optoelectronic devices.

Methods

Materials

Lead iodide (PbI_2, 99.99%), lead bromide ($PbBr_2$, 99.99%), methylammonium iodide (MAI) and formamidinium iodide (FAI) were purchased from Advanced Election Technology Co., Ltd. Caesium iodide (CsI, >99.0%), guanidine thiocyanate (GuaSCN, >99.0%), bathocuproine (BCP, >99.0%), dibutyl sulfoxide (DBSO, >96.0%) and [4-(3,6-dime-thyl-9H-carbazol-9-yl)butyl]phosphonic acid (Me-4PACz, >99.0%) were purchased from TCI chemicals. PEDOT:PSS aqueous solution (Al-4083), ethylenediammonium diiodide ($EDAI_2$, 99.99%), fullerene (C_{60}, 99%), and 1,3-propanediamine dihydriodide ($PDAI_2$, 99.99%) were purchased from Xi'an Yuri Solar Co., Ltd. Potassium iodide (KI, >99.0%), glycine hydrochloride (GlyHCl, ≥99%), tin(II) fluoride (SnF_2, 99%), and tin(II) iodide (SnI_2, beads, 99.99%, trace metals basis) were purchased from Sigma-Aldrich. Tetrakis(dimethylamino) tin (IV) (99.9999%) for atomic layer deposited (ALD) SnO_x was bought from Nanjing Ai Mou Yuan Scientific Equipment Co., Ltd. MSN and MSN-SH dispersions (100 nm, 50 mg mL^{-1} in isopropanol) were purchased from Haian Zhichuan Battery Material Technology Co., Ltd. The process of functionalization of MSN into MSN-SH was similar to that previously reported[47]. Al_2O_3 dispersion (100 nm, 20 wt% in isopropanol) was purchased from Macklin. Unless stated, otherwise, all solvents were purchased from Sigma-Aldrich. All materials were used as received without further purification.

Perovskite precursor solution

WBG $FA_{0.8}Cs_{0.2}Pb(I_{0.6}Br_{0.4})_3$ perovskite. The precursor solution (1.2 M) was prepared by dissolving 0.96 mmol FAI, 0.24 mmol CsI, 0.48 mmol PbI_2, 0.72 mmol $PbBr_2$, and 0.024 mmol KI in mixed solvents of DMF and DMSO with a volume ratio of 3:1 and stirred at room temperature overnight.

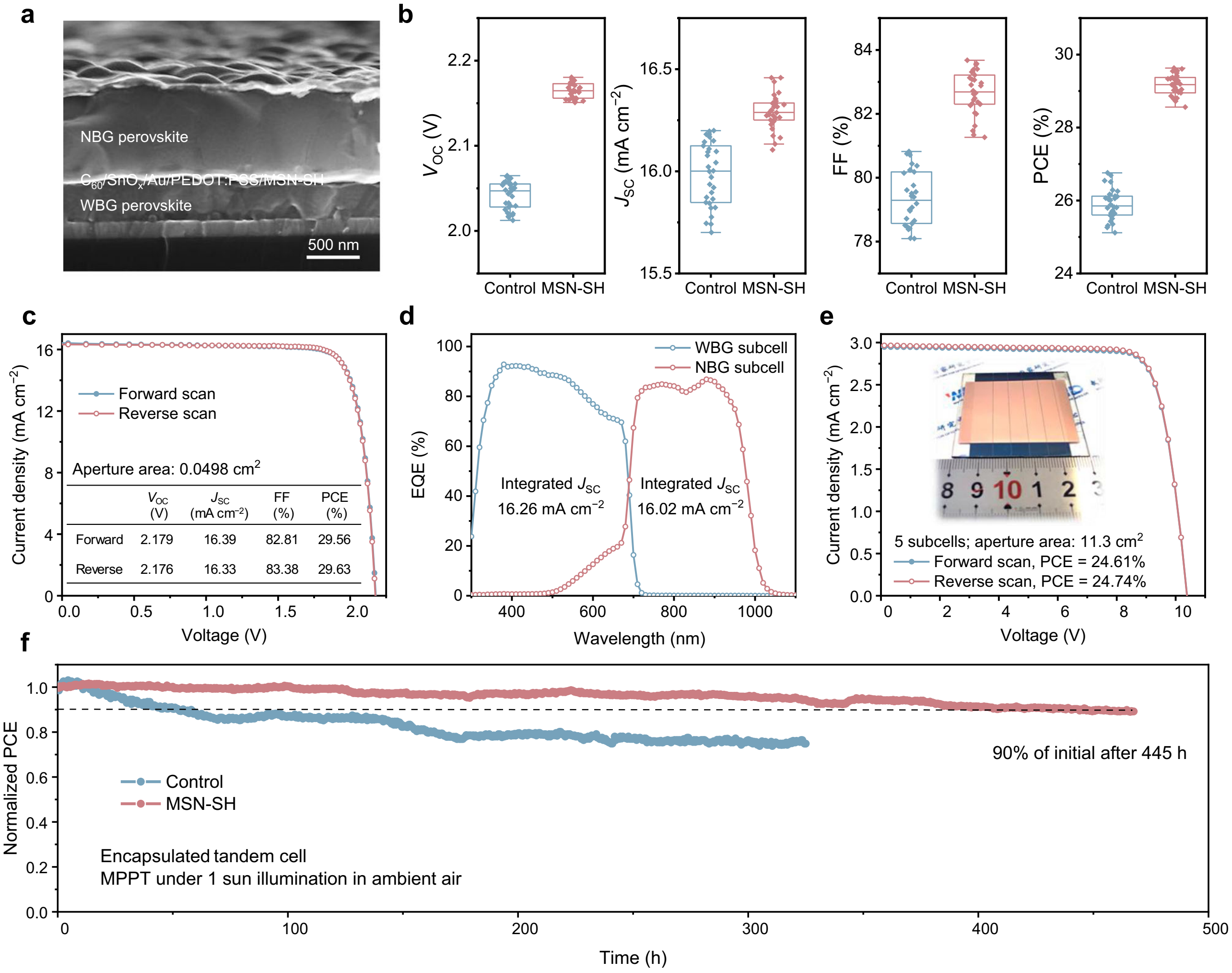

Fig. 4 | All-perovskite tandem solar cells. a Cross-sectional SEM image of the all-perovskite tandem device. **b** Statistical distribution of the photovoltaic parameters for control and MSN-SH tandems based on 30 devices. **c** *J*–*V* curves of the best-performing tandem device with an aperture area of 0.0498 cm². **d** EQE spectra of WBG and NBG subcell within the tandem device. **e**, *J*–*V* curves of the champion tandem mini-module with an aperture area of 11.3 cm². (Inset) Photograph of the tandem mini-module. **f** Continuous MPPT for the encapsulated tandem device under simulated AM1.5 G illumination in ambient air. Source data are provided as a Source Data file.

NBG $Cs_{0.1}FA_{0.6}MA_{0.3}Pb_{0.5}Sn_{0.5}I_3$ perovskite. The precursor solution (2.0 M) was prepared by dissolving 1.2 mmol FAI, 0.6 mmol MAI, 0.2 mmol CsI, 1.0 mmol PbI_2, 1.0 mmol SnI_2, 0.1 mmol SnF_2, 0.04 mmol GuaSCN and 0.04 mmol GlyHCl in mixed solvents of DMF and DMSO with a volume ratio of 3:1. The precursor solution was stirred at 45 °C for 1 h and then filtered using a 0.22-µm PTFE membrane before use.

1.68 eV-bandgap $FA_{0.8}Cs_{0.2}Pb(I_{0.8}Br_{0.2})_3$ perovskite. The precursor solution (1.5 M) was prepared by dissolving 1.2 mmol FAI, 0.3 mmol CsI, 1.05 mmol PbI_2, 0.45 mmol $PbBr_2$ and 0.03 mmol KI in mixed solvents of DMF and DMSO with a volume ratio of 3:1 and stirred overnight.

1.52 eV-bandgap $FA_{0.98}Cs_{0.02}PbI_3$ perovskite. The precursor solution (1.5 M) was prepared by dissolving 1.47 mmol FAI, 0.03 mmol CsI, 1.5 mmol PbI_2 and 0.15 mmol DBSO in mixed solvents of DMF and NMP with a volume ratio of 6:1 and stirred overnight.

Device fabrication

NBG PSCs. Glass/ITO substrates were consecutively cleaned by sequential ultrasonication for 15 min with detergent solution, deionized water, and ethanol. The cleaned substrates were dried with high-pressure N_2 gas flow and then were cleaned by UV-ozone treatment for 30 min. The PEDOT:PSS solution was spin-coated onto the ITO substrate at 5000 rpm for 30 s, then annealed at 150 °C for 20 min in ambient air and finally transferred into an N_2-filled glovebox before use. For the MSN-SH modified layer, MSN-SH dispersions (20 mg mL^{-1}) were dropped on the HTL and spin-coated at 2000 rpm for 30 s, followed by annealing at 100 °C for 10 min. The 60 µL of perovskite solution was spin-coated onto the substrate with the two-step process (1000 rpm for 10 s and 4000 rpm for 40 s). Then 350 µL of chlorobenzene (CB) was quickly dropped onto the centre of the spinning substrate during the second spin-coating step at 20 s before the end of the procedure. The substrates were then thermally annealed at 100 °C for 10 min. For the passivation layer, $EDAI_2$ (0.5 mg in 1 mL IPA and toluene mixed solvent at the volume ratio of 1:1, filtered before use) was spin-coated on top of perovskite films at 4000 rpm for 20 s and annealed at 100 °C for 5 min. Finally, 20 nm C_{60}, 5 nm BCP, and 100 nm Ag were sequentially thermally evaporated under a high vacuum ($<5\times10^{-4}$ Pa).

WBG PSCs. Me-4PACz (0.8 mg mL^{-1}) dissolved in ethanol was spin-coated on the ITO substrates at 3000 rpm for 25 s and then annealed at 100 °C for 10 min. The MSN-SH dispersion (20 mg mL^{-1}) was deposited by spin-coating at 2000 rpm for 30 s, followed by annealing at 100 °C for 10 min. Then the perovskite solution was spin-coated on the substrate at 5000 rpm for 60 s with an acceleration of 1000 rpm s^{-1}, during which 400 μL ethyl acetate was dripped onto the center of film at 30 s before the end of spin-coating. The as-coated precursor films were subsequently annealed on a hotplate at 100 °C for 10 min. After cooling down, 100 μL of $PDAI_2$ (1.5 mg mL^{-1} in IPA) solution was spin-coated onto the as-prepared perovskite films at 4000 rpm for 20 s with an acceleration of 3000 rpm s^{-1} and annealed at 100 °C for 5 min. The deposition of C_{60}/BCP/Ag was the same as described in the NBG PSCs.

All-perovskite tandem devices. For the WBG subcell, the deposition of Me-4PACz, MSN-SH dispersion, perovskite film, $PDAI_2$, and C_{60} layers were the same as WBG PSCs. Then the films were transferred to the ALD chamber to deposit 30 nm SnO_x at 100 °C using precursors of tetrakis(dimethylamino) tin (IV) (99.9999%) and deionized water. After SnO_x deposition, the substrates were transferred to the evaporation chamber to deposit 1 nm Au. Next, the diluted PEDOT:PSS solution with IPA at a volume ratio of 1:2 was spin-coated onto the WBG subcell at 4000 rpm for 30 s, followed by annealing at 100 °C for 15 min in the ambient. After the samples were transferred to an N_2-filled glovebox, the MSN-SH dispersion, perovskite films, $EDAI_2$, C_{60}, BCP, and Ag electrodes were deposited in full accordance with the above sequence of NBG PSCs preparation process. Finally, the all-perovskite tandem solar cell with an architecture of glass/ITO/Me-4PACz/MSN-SH/WBG perovskite (~350 nm)/$PDAI_2$/C_{60}/ALD-SnO_x (30 nm)/Au (1 nm)/PEDOT:PSS/MSN-SH/NBG perovskite (~900 nm)/$EDAI_2$/C_{60}/BCP/Ag was successively prepared.

1.68 eV-bandgap PSCs. The preparation process was the same as that of the WBG PSCs.

1.52 eV-bandgap PSCs. The deposition of Me-4PACz, MSN-SH dispersions was the same as for WBG PSCs. The perovskite solution was spin-coated on the substrate at 5000 rpm for 60 s. At the 12th second of spinning, 500 μL of ethyl acetate was dripped onto the centre of the substrate. The as-coated precursor films were subsequently annealed on a hotplate at 130 °C for 15 min. Then 100 μL of 3,5-bis(trifluoromethyl)phenethylammonium iodide[44] (1 mg mL^{-1} in IPA) were spin-coated onto the as-prepared perovskite films at 5000 rpm for 30 s; the films were subsequently dried at 100 °C for 5 min. The deposition of C_{60}/BCP/Ag was the same as described in the WBG PSCs.

Mini-modules fabrication. As illustrated in Supplementary Fig. 40, the mini-modules were fabricated on the 5.0 cm × 5.0 cm sized glass/ITO substrate using a 532 nm nanosecond laser scribing with a power of 4 W to form P1 lines isolated subcells with a width of 6.8 mm. The preparation process of the mini-module is the same as that of the above small-area devices, the only difference is that the acceleration in all spin-coating processes needs to be changed to 1000 rpm s^{-1} to ensure that the solution can be evenly coated on the substrate. To prevent the oxidation of NBG perovskite when exposed to ambient air, we deposited ALD-SnO_x with a thickness of 10 nm on the C_{60} layer before the P2 scribing (0.5 W) as previously reported[48]. Then the Cu (100 nm) based metal electrode was deposited. Finally, effective monolithically interconnected modules were formed by laser scribing (0.5 W) to form P3 lines. For module encapsulation, the connection was extended by attaching tinned copper ribbon strips to metal electrodes. The edge of the sealing glass was sealed with butyl tape with a width of approximately 0.5 cm, and vacuum lamination was performed using an industrial laminator at 100 °C for 10 min. All encapsulation operations were completed in an N_2-filled glovebox.

Mechanical strength measurements

Stress-displacement curve measurements were performed on an electronic universal testing machine (LGD-500) by using the double-cantilever beam delamination technique[37]. The samples adopted a device structure of glass/ITO/PEDOT:PSS/perovskite/UV epoxy/glass with a substrate size of 1.3 × 1.5 cm^2. Perovskite films with and without MSN or MSN-SH layer were prepared on PEDOT:PSS-coated ITO/glass as described above. Then, UV epoxy was coated on a 1 × 1 cm^2 glass substrate and adhered to the centre of the perovskite films, followed by UV solidification for 1 min. The samples were mounted on a tensile test fixture and stretched at an operating rate of 0.5 mm min^{-1} to delaminate the interface. To calculate the specific fracture energy (W), the following equation is used: $W = \int \sigma d\varepsilon$, where σ is the measured stress and ε is the measured strain.

Computational details

The first-principle-based geometry optimization calculations were carried out within density-functional theory (DFT), implemented in the Vienna Ab Initio Simulation Package (VASP) code[49], using the frozen-core projector augmented-wave (PAW) method to describe the interaction between the atomic cores and the valence electron density[50]. The exchange-correlation potential was approximated within the generalized gradient approximation (GGA) using the Perdew-Burke Ernzerhof (PBE) functional[51]. The dispersion-corrected DFT-D3 schemes were employed to describe the Van der Waals (vdW) interactions[52]. Plane-wave cutoff energy was set to 500 eV. The conjugate gradient algorithm was used in ionic optimization, convergence threshold was set to 10^{-5} eV $atom^{-1}$ in electronic relaxation and below 0.3 eV $Å^{-1}$ in Hellmann–Feynman force on each atom. We have constructed the slab model of the (001) crystal plane with 3*3*2 supercell, where the vacuum layer was set to 20 Å. The three atom layers of the slab model were fixed from bottom to top as a bulk phase structure, including two atom layers with Pb and Sn mixed configuration, and one-layer organic molecules between the atoms layer of Pb and Sn mixed configuration. The rest of the one-atom layer with Pb and Sn mixed configuration and one-layer organic molecules were relaxed as surface structures. The Brillouin zone in reciprocal space was sampled by a Γ-centered Monkhorst–Pack scheme with 1 × 1 × 1 k-point grids for geometry optimization, due to the $a = b = 18.95$ Å of lattice parameters for the slab model of (001) crystal plane[53]. The climbing image nudged elastic band (CI-NEB) method was used to estimate the diffusion barrier of the I atom. The models of transition state calculation were constructed with seven I atoms using the linear interpolation method, and then the VASP program based on the CI-NEB method was implemented to converge the transition and intermediate states[54]. The positions of I atoms were continuously optimized to obtain the empirically reasonable transition and intermediate states.

Device characterization

The *J–V* curves of the devices were measured using a Keithley 2400 source measurement unit and a solar simulator (Oriel, model 9119) with an AM1.5 G spectrum. The light intensity was calibrated using a certified WPVS standard silicon reference cell (Enlitech) at 100 mW cm^{-2}. The aperture area of devices was determined by the black masks of 0.0498 cm^2, 0.0930 cm^2, and 11.3 cm^2 area. The stabilized power output was achieved by monitoring the stabilized current density output under MPP bias voltage (extracted from the reverse scan *J-V* curves). EQE spectra were performed in ambient air using a QE system (Enlitech Co., Ltd.). For EQE measurements of tandem solar cells, two highly bright LEDs with emission peaks of 850 and 460 nm were used for the measurements of the WBG and NBG subcells, respectively. The Transient photovoltage (TPV), transient photocurrent (TPC), and Mott-Schottky plots were obtained by a Zennium electrochemistry workstation (Zahner, Germany). External electroluminescence quantum efficiency (EQE_{EL}) measurement was measured on ELCT-3010 (Enlitech Co., Ltd.). The operational stability tests were carried out under AM1.5G solar simulator illumination source (Beijing Saifan Photoelectric Instrument Co., Ltd.) with an intensity of 100 mW cm^{-2} using a maximum power point tracking system (Wuhan Jiuyao Optoelectronic Technology Co., Ltd.) in ambient conditions.

Films characterization

SEM images were taken with a Nova NanoSEM 450 scanning electron microscope at 10 kV operating voltage. XRD spectra were measured on an X-ray diffractometer (PANalytical B.V. Co.) with Cu K_α radiation. The GIWAXS measurements were performed at beamline BL14B1 of the Shanghai Synchrotron Radiation Facility. The wavelength of X-rays was 1.24 Å (10 KeV), and diffraction patterns were collected by using a two-dimensional Mar225 detector with different incidence angles and 30 s exposure times. The GIXRD patterns were acquired by using a Rigaku Smartlab with Cu K_α radiation in the 2θ range of 30.6 to 32.6°. The FLIM images were measured by FLIM300. TRPL measurements were conducted by HORIBA DeltaFlex spectrometer. The in-situ PL measurements were conducted with laser excitation at 532 nm and the area of interest was fixed on the micro-spectral measurement system (ProSp-Micro40-VIS), together with spectrograph (Ocean Insight, USA). Absorption spectra were measured using a Lambda 950 UV-vis spectrophotometer (PerkinElmer Co., USA). XPS was measured with a monochromatic Al K_α X-ray source (1486.6 eV) operating at 100 W (Thermo ESCALAB 250XI). Quasi-Fermi level splitting (QFLS) values were calculated by the data extracted from photoluminescence quantum yield (PLQY) measurements using QuantaMaster 8000 (HORIBA, Canada) with an 808 nm laser to photoexcite the films placed in an integrating sphere. The laser intensity was adjusted to 1 sun equivalent intensity using a PSC to obtain a current density at 0 V equal to its J_{SC}.

Reporting summary

Further information on research design is available in the Nature Portfolio Reporting Summary linked to this article.

Data availability

The main data in this study are available within the published article and its supplementary information and source data files. Additional data are available from the corresponding author upon request. Source data are provided in this paper. Source data are provided with this paper.

References

1. Eperon, G. E. et al. Perovskite-perovskite tandem photovoltaics with optimized band gaps. *Science* **354**, 861–865 (2016).
2. Eperon, G. E., Hörantner, M. T. & Snaith, H. J. Metal halide perovskite tandem and multiple-junction photovoltaics. *Nat. Rev. Chem.* **1**, 0095 (2017).
3. Leijtens, T., Bush, K. A., Prasanna, R. & McGehee, M. D. Opportunities and challenges for tandem solar cells using metal halide perovskite semiconductors. *Nat. Energy* **3**, 828–838 (2018).
4. Jošt, M., Kegelmann, L., Korte, L. & Albrecht, S. Monolithic perovskite tandem solar cells: a review of the present status and advanced characterization methods toward 30% efficiency. *Adv. Energy Mater.* **10**, 1904102 (2020).
5. Wang, R. et al. Prospects for metal halide perovskite-based tandem solar cells. *Nat. Photonics* **15**, 411–425 (2021).
6. Green, M. A. et al. Solar cell efficiency tables (Version 64). *Prog. Photovolt.* **32**, 425–441 (2024).
7. Shockley, W. & Queisser, H. J. Detailed balance limit of efficiency of p-n junction solar cells. *J. Appl. Phys.* **32**, 510–519 (1961).
8. Ramadan, A. J., Oliver, R. D. J., Johnston, M. B. & Snaith, H. J. Methylammonium-free wide-bandgap metal halide perovskites for tandem photovoltaics. *Nat. Rev. Mater.* **8**, 822–838 (2023).
9. Hu, S. et al. Narrow bandgap metal halide perovskites for all-perovskite tandem photovoltaics. *Chem. Rev.* **124**, 4079–4123 (2024).
10. Lin, R. et al. All-perovskite tandem solar cells with 3D/3D bilayer perovskite heterojunction. *Nature* **620**, 994–1000 (2023).
11. Chen, H. et al. Regulating surface potential maximizes voltage in all-perovskite tandems. *Nature* **613**, 676–681 (2022).
12. He, R. et al. Improving interface quality for 1-cm^2 all-perovskite tandem solar cells. *Nature* **618**, 80–86 (2023).
13. Pan, Y. et al. Surface chemical polishing and passivation minimize non-radiative recombination for all-perovskite tandem solar cells. *Nat. Commun.* **15**, 7335 (2024).
14. Yang, F. & Zhu, K. Advances in mixed tin-lead narrow-bandgap perovskites for single-junction and all-perovskite tandem solar cells. *Adv. Mater.* **36**, 2314341 (2024).
15. Hu, S. et al. Mixed lead-tin perovskite films with >7 μs charge carrier lifetimes realized by maltol post-treatment. *Chem. Sci.* **12**, 13513–13519 (2021).
16. Pascual, J. et al. Origin of Sn(ii) oxidation in tin halide perovskites. *Mater. Adv.* **1**, 1066–1070 (2020).
17. Hu, S. et al. Optimized carrier extraction at interfaces for 23.6% efficient tin–lead perovskite solar cells. *Energy Environ. Sci.* **15**, 2096–2107 (2022).
18. Gao, H. et al. Homogeneous crystallization and buried interface passivation for perovskite tandem solar modules. *Science* **383**, 855–859 (2024).
19. Wang, J. et al. Bimolecular crystallization modulation boosts the efficiency and stability of methylammonium-free tin-lead perovskite and all-perovskite tandem solar cells. *Adv. Energy Mater.* **14**, 2402171 (2024).
20. Wang, J. et al. Halide homogenization for low energy loss in 2-eV-bandgap perovskites and increased efficiency in all-perovskite triple-junction solar cells. *Nat. Energy* **9**, 70–80 (2023).
21. Prasanna, R. et al. Design of low bandgap tin–lead halide perovskite solar cells to achieve thermal, atmospheric and operational stability. *Nat. Energy* **4**, 939–947 (2019).
22. Chen, B. et al. Bifacial all-perovskite tandem solar cells. *Sci. Adv.* **8**, eadd0377 (2022).
23. Lee, S. et al. Buried interface modulation via PEDOT:PSS ionic exchange for the Sn-Pb mixed perovskite based solar cells. *Chem. Eng. J.* **479**, 147587 (2024).
24. Zhu, J. et al. Custom-tailored hole transport layer using oxalic acid for high-quality tin-lead perovskites and efficient all-perovskite tandems. *Sci. Adv.* **10**, eadl2063 (2024).
25. Luo, C. et al. Engineering the buried interface in perovskite solar cells via lattice-matched electron transport layer. *Nat. Photonics* **17**, 856–864 (2023).
26. Hu, H. et al. Void-free buried interface for scalable processing of p-i-n-based $FAPbI_3$ perovskite solar modules. *Joule* **7**, 1574–1592 (2023).
27. Chen, S. et al. Stabilizing perovskite-substrate interfaces for high-performance perovskite modules. *Science* **373**, 902–907 (2021).
28. Deng, W. et al. Super hydrophilic, ultra bubble repellent substrate for pinhole free Dion–Jacobson perovskite solar cells. *Appl. Phys. Lett.* **121**, 233902 (2022).
29. Chen, S. et al. Crystallization in one-step solution deposition of perovskite films: Upward or downward? *Sci. Adv.* **7**, eabb2412 (2021).
30. Kim, K.-J. et al. Inspection of substrate-heated modified PEDOT:PSS morphology for all spray deposited organic photovoltaics. *Sol. Energy Mater. Sol. Cells* **94**, 1303–1306 (2010).
31. Wei, D. et al. A TiO_2 embedded structure for perovskite solar cells with anomalous grain growth and effective electron extraction. *J. Mater. Chem. A* **5**, 1406–1414 (2017).
32. Peng, W. et al. Reducing nonradiative recombination in perovskite solar cells with a porous insulator contact. *Science* **379**, 683–690 (2023).
33. Ball, J. M., Lee, M. M., Hey, A. & Snaith, H. J. Low-temperature processed meso-superstructured to thin-film perovskite solar cells. *Energy Environ. Sci.* **6**, 1739–1743 (2013).

34. Gao, Y. et al. Elimination of unstable residual lead iodide near the buried interface for the stability improvement of perovskite solar cells. *Energy Environ. Sci.* **16**, 2295–2303 (2023).
35. Fei, C. et al. Lead-chelating hole-transport layers for efficient and stable perovskite minimodules. *Science* **380**, 823–829 (2023).
36. Xiao, T. et al. Elimination of grain surface concavities for improved perovskite thin-film interfaces. *Nat. Energy* **9**, 999–1010 (2024).
37. Leng, X. et al. Mechanical strengthening of a perovskite-substrate heterointerface for highly stable solar cells. *Energy Environ. Sci.* **17**, 4295–4303 (2024).
38. Cui, H. et al. Lead halide coordination competition at buried interfaces for low V_{OC}-deficits in wide-bandgap perovskite solar cells. *Energy Environ. Sci.* **16**, 5992–6002 (2023).
39. Al-Ashouri, A. et al. Monolithic perovskite/silicon tandem solar cell with >29% efficiency by enhanced hole extraction. *Science* **370**, 1300–1309 (2020).
40. Liu, S. et al. Buried interface molecular hybrid for inverted perovskite solar cells. *Nature* **632**, 536–542 (2024).
41. Lu, X. et al. Dynamic reversible oxidation-reduction of iodide ions for operationally stable perovskite solar cells under ISOS-L-3 protocol. *Adv. Mater.* **36**, 2400852 (2024).
42. Dai, Z. et al. Interfacial toughening with self-assembled monolayers enhances perovskite solar cell reliability. *Science* **372**, 618–622 (2021).
43. Yu, Z. et al. Solution-processed ternary tin (II) alloy as hole-transport layer of Sn-Pb perovskite solar cells for enhanced efficiency and stability. *Adv. Mater.* **34**, 2205769 (2022).
44. Chen, R. et al. Reduction of bulk and surface defects in inverted methylammonium- and bromide-free formamidinium perovskite solar cells. *Nat. Energy* **8**, 839–849 (2023).
45. Rau, U. Reciprocity relation between photovoltaic quantum efficiency and electroluminescent emission of solar cells. *Phys. Rev. B* **76**, 085303 (2007).
46. Li, Z. et al. Stabilized hole-selective layer for high-performance inverted p-i-n perovskite solar cells. *Science* **382**, 284–289 (2023).
47. Zhang, J. et al. Synthesis of graphene from dry ice in flames and its application in supercapacitors. *Chem. Phys. Lett.* **591**, 78–81 (2014).
48. Xiao, K. et al. Scalable processing for realizing 21.7%-efficient all-perovskite tandem solar modules. *Science* **376**, 762–767 (2022).
49. KresseFurthmuller Efficient iterative schemes for ab initio total-energy calculations using a plane-wave basis set. *Phys. Rev. B Condens. Matter* **54**, 11169–11186 (1996).
50. Kresse, G. & Joubert, D. From ultrasoft pseudopotentials to the projector augmented-wave method. *Phys. Rev. B* **59**, 1758–1775 (1999).
51. Perdew, J. P., Burke, K. & Ernzerhof, M. Generalized gradient approximation made simple. *Phys. Rev. Lett.* **78**, 1396–1396 (1997).
52. Grimme, S., Antony, J., Ehrlich, S. & Krieg, H. A consistent and accurate ab initio parametrization of density functional dispersion correction (DFT-D) for the 94 elements H-Pu. *J. Chem. Phys.* **132**, 154104–154123 (2010).
53. Monkhorst, H. J. & Pack, J. D. Special points for Brillouin-zone integrations. *Phys. Rev. B* **13**, 5188–5192 (1976).
54. Norskov, J. K. et al. Origin of the overpotential for oxygen reduction at a fuel-cell cathode. *J. Phys. Chem. B* **108**, 17886–17892 (2004).

Acknowledgements

W.C. acknowledges the financial support from the National Natural Science Foundation of China (W2412077, U20A20252), the Innovation Project of Optics Valley Laboratory (OVL2021BG008) and the Ministry of Science and Technology of China (2021YFB3800104). Z.L. acknowledges the financial support from the National Natural Science Foundation of China (52473301), the Natural Science Foundation of Hubei Province (2022CFA093), the Self-determined and Innovative Research Funds of HUST (2020kfyXJJS008) and the Young Elite Scientists Sponsorship Program by CAST. J.W. acknowledges the financial support from the Fundamental Research Funds for the Central Universities, HUST (2023JYCXJJ041). R.C. acknowledges the financial support from China Postdoctoral Science Foundation (2023M731172). Q.Z. acknowledges the financial support from China Postdoctoral Science Foundation (2024M751002, GZC20240528). Zhiguo Z. and X.Q. acknowledges the Scientific Research Foundation of China Huaneng Group (HNKJ22-H104, HNKJ21-H26). H.J.S. acknowledges the financial support from the Engineering and Physical Sciences Research Council (EPSRC), U.K., under Grant numbers EP/S004947/1, EP/X038777/1, EP/X037169/1, and EP/T028513/1, the European Union's Horizon Europe research and innovation programme under Grant agreement no. 101075330 of the NEXUS project. S.H. acknowledges the financial support from the JST-Mirai Program (JPMJMI22E2), NEDO, the International Collaborative Research Program of ICR, Kyoto University. Junke W. acknowledges the financial support from the Marie Skłodowska Curie Actions Postdoc Fellow (UKRI Guarantee, grant number EP/Y029216/1). For funding from the European Union, views and opinions expressed are, however, those of the author(s) only and do not necessarily reflect those of the European Union or RIA. Neither the European Union nor the granting authority can be held responsible for them. The authors thank the Analytical and Testing Center of HUST for the facilities' support of sample measurements.

Author contributions

J.W., S.H., H.Z., S.L. and Z.Z. contributed equally to this work. W.C., Z.L., and H.J.S. conceived the idea and directed the overall project. J.W., S.H., H.Z., and C.S. fabricated the devices. J.W., S.L., R.C., C.S., J.Z., W.L., Y.P., and Q.Z. carried out the film and device characterizations. Sibo L. and L.Q. carried out the GIXRD measurements. G.Z. carried out the GIWAXS measurements. R.C. and F.R. helped with device encapsulation and module fabrication. S.Y. carried out the mechanical strength measurements. Z.Z., B.L., and N.L. conducted the DFT calculations. S.H., Junke W., Sibo L., R.C., X.L., H.R., Q.Z., N.L., J.L., L.Q., X.Q. and Zhiguo Z. contributed to analyzing data and providing useful suggestions for the manuscript. J.W., S.H., H.Z., and S.L. prepared the manuscript under the supervision of A.W., Z.L., H.J.S., and W.C. All authors discussed the results and commented on the written manuscript.

Competing interests

H.J.S. is the co-founder and CSO of Oxford PV Ltd. and Helio Display Materials Ltd. A.W. is the co-founder and CSO of Enecoat Technologies Co., Ltd. The other authors declare no competing interests.

Additional information

Supplementary information The online version contains supplementary material available at https://doi.org/10.1038/s41467-025-59891-z.

Correspondence and requests for materials should be addressed to Zonghao Liu, Henry J. Snaith or Wei Chen.

Peer review information *Nature Communications* thanks Tzu-Chien Wei, the other, anonymous, reviewer(s) for their contribution to the peer review of this work. A peer review file is available.